Fine-tuned photochromic WO3-x thin films: A detailed study from structural analysis to UV photo-sensing application

Yazan Badour, Sylvain Danto, Mathieu Gonidec, Christine Labrugère, Matthew Suchomel, Gilles Philippot, Manuel Gaudon

Fine-tuned photochromic WO_{3-x} thin films: A detailed study from structural analysis to UV photo-sensing application

Yazan Badour, Sylvain Danto, Mathieu Gonidec, Christine Labrugère, Matthew R. Suchomel, Gilles Philippot, Manuel Gaudon *

CNRS, Univ. Bordeaux, Bordeaux INP, ICMCB (UMR 5026), Pessac, F-33600, France

Keywords:
Tungsten oxides
Nano
Photochromism
Sensors
Photo-batteries
UV-Sensing

A B S T R A C T

The oxygen substoichiometry of as-prepared WO_3 (tungsten trioxide) nano-powders (NPs) from a polyol process was tuned via peptization of the NPs in aqueous solutions of different $Cr_2O_7^{2-}$ oxidizing concentrations. The as-synthesized materials have been characterized by X-ray scattering (XRD and PDF), transmission electron microscopy (TEM), X-ray photoelectron (XPS), and UV-VIS photochromic activity. The local atomic structure of WO_{3-X} was investigated using total scattering atomic pair distribution function (PDF) analysis based on X-ray total scattering data collected on powder at ambient conditions. The PDF analysis confirms that the crystal structure of all studied samples can be described in terms of very small crystallites with a P21/n space-group monoclinic framework but with anomalous unit cell distortion parameters, indicating that small crystallite sizes resulted in a larger monoclinic distortion (as measured by the beta angle of the unit cell). The nanometer dimension of the crystallites combined as well as the oxygen-tungsten stoichiometric ratio control, are key features for optimized photochromic properties. Moreover, we present the fabrication of a WO_{3-x} thin film based UV photosensor, which was carried out on silica glass substrates via the dip-coating method. The obtained films exhibited a UV photoresponse and photoelectric characteristics at 5 V bias voltages able to detect very low UV doses, inferior to 10 W/m^2. The photo-detection measurements prove the usability of our device as a UV photodetector with a good responsivity of 0.37 A/W and external quantum efficiency of more than 100% even at a very low power density (9.2 W/m^2) of UV illumination.

1. Introduction

Stoichiometric WO_3 (tungsten trioxide) is an n-type indirect band gap semiconductor, with a band gap ranging from 2.6 to 3.52 eV [1]. The prototype crystal structure of WO_3 is cubic ReO_3, which builds up a three-dimensional network by corner-sharing of the WO_6-octahedra [2]. Each W atom, lying off-center, is surrounded by a regular octahedron of six nearest O atoms with twisted chain organization [2]. Thus, tungsten trioxide WO_3 occurs, depending on the amplitude and the direction of the twist angle, sequentially in six additional phases which have been identified as follows: monoclinic II (ε-WO_3), triclinic (δ-WO_3), monoclinic I (γ-WO_3), orthorhombic (β-WO_3), tetragonal (α- WO_3) and hexagonal (h-WO_3) [2,3]. WO_3 is also known for its nonstoichiometric compositions (WO_{3-x}, where $0 < x \leq 1$) [4,5]. The wide existence of these nonstoichiometric structures is due to the WO_{3-x} lattice that can withstand a considerable number of O vacancies, therefore resulting in the formation of different W oxidation states. WO_{3-x} compositions which vary from $WO_{2.625}$ ($W_{32}O_{84}$) to $WO_{2.96}$ can be described as local condensation producing edge-sharing octahedral site organization arising from the pure corner-sharing networks of the WO_6 octahedral in stoichiometric WO_3 [6,7]. Tungsten oxide films have been prepared by a variety of methods, such as thermal evaporation, chemical vapor deposition, sputtering and dip-coating methods [8–10]. Until now, nearly all of its applications are in the photo- and electrochromic "smart" windows, erasable optical-storage devices, catalysts, gas sensors, and humidity or temperature sensors [11–14]. Regarding more particularly the photochromism of tungsten oxide, Deb was the first to highlight the photochromism of WO_3 thin films, in 1973 [15]. Despite a weak optical contrast between colored and bleached states as well as its very slow and frequently incomplete bleaching process (lack of adequate reversibility for many applications), WO_3 is more and more studied. Indeed, from the optimization of crystallite morphologies and/or the

* Corresponding author.
E-mail address: manuel.gaudon@icmcb.cnrs.fr (M. Gaudon).

tungsten/oxygen stoichiometry, recent studies have been carried out showing a particular interest in producing photosensitive and reprintable inks based on WO_3 nanoparticles [11,16]. Now it is well established that the blue color in WO_3 issuing from the photo-reduction of the material is based on the transfer of electrons between tungsten ions having different valence states (W^{6+}, W^{5+}) via an intervalence charge transfer (IVCT) [17,18]. The photo-redox process in this material follows the steps described subsequently. When the WO_3 film is irradiated with UV light, electrons (e^-) and holes (h^+) are generated (excitons). Then sufficiently long charge depletion occurs, allowing some few electrons to be trapped by some tungsten ions, leading to W^{5+} ion formation, thus leading to IVCT phenomenon and blue coloration. IVCT is associated with the creation of convoluted absorption bands at the frontier between the visible range and the near-infrared, resulting in the blue coloration of the material [19]. Recent studies have shown that reversible photochromism in WO_3 is enhanced by the presence of oxygen vacancies and/or could be activated by cations (Cu, for illustration) doping [20,21]. Our previous works have allowed the preparation from controlled germination in polyol medium of clear blue colored, nanometric and oxygen-deficient WO_{3-x} with intense (in terms of visible or NIR contrast between colored and bleached states), reversible and fast photochromism [12,22,23]. In this current paper, the first part addresses the optimization of the photochromic contrasts by oxidizing the clear blue WO_{3-x} crystallite to get yellow starting compounds (in other words; a rapid intense blueish photochromism under UV irradiation). In this first part, we also discuss the initial color, the crystallographic structure, the morphology, and the chemical composition of as-prepared nanoparticles varying the oxidizer dosage, using different characterization techniques as UV–Vis spectroscopy, X-ray diffraction, SEM investigations, and XPS spectroscopy. A section is devoted to PDF analysis which leads, for such very nanometric crystallites, to more accurate information on the periodic atomic organization than powder X-ray diffraction. The second part of this paper is devoted to the photochromic properties of the various as-prepared samples.

Beyond photochromic properties, the current paper also proposes to explore the exploitation of the change of conductivity of the tungsten oxide particles with the photoredox reaction. While ZnO, GaN, and NiO are used in UV photodetectors, there are few reports on tungsten oxide (WO_3) as a UV photodetector [24]. Exposure to UV radiation can do serious damage to humans including deformation of DNA structure, attacking the immune system, and increasing skin photoaging, leading to an increasing number of skin cancer cases [25]. From this point of view, UV photodetectors have an important role in health care and therefore, they are in high demand. In the work of D. Shao et al. [26], they fabricated a UV photodetector from the 3D WO_3 nanoscale. The UV sensor showed a good photoresponsivity (5.1 A/W), which was attributed to the surface oxygen adsorption–desorption process as well as the high surface to volume ratio of the 3D nanoscale structure. Furthermore, in the work of K. Huang et al. [27], the UV photo-conducting properties of a single hexagonal WO_3 nanowire were studied. They suggested that the photo-conducting mechanism can be attributed to the hole-trapping through adsorption and desorption of oxygen molecules on the surface of the WO_3 nanowire. Hence, on this basis, in the third and final part of the present work, we report the fabrication and characterization of WO_{3-x} -based thin film for UV sensing properties.

2. Materials and methods

2.1. Polyol synthesis of WO_3 powders

Chemical reagents were purchased from Sigma Aldrich and used as received. Tungsten (VI) chloride was used as a tungsten source, diethylene glycol (DEG) as solvent, and potassium dichromate, $K_2Cr_2O_7$ as an oxidizer agent. The WO_3 was synthesized by the polyol method as reported in our previous papers [21,28]. The as-obtained raw powders were oxidized by introduction into an aqueous solution where the strong oxidizer was previously solubilized. The raw powder and a series of oxidized powders with different oxidizer dosages (0, 0.005, 0.01, 0.02 M) were prepared and named: WOR, WOX1, WOX2, and WOX3, respectively. For comparison, one submicronic particle sized powder (WOT sample) was prepared by calcination under air at 600 °C of the WOR sample.

2.2. Pristine film elaboration

The raw and oxidized nanoparticles (NPs) were separately dispersed in ethanol to prepare the suspensions (weight content in NPs is 90 g L^{-1}). Then the suspensions were dip-coated on a standard glass substrate to obtain pristine and doped thin films. The dip-coating parameters are (i) the dip-coating speed: 133 mm min^{-1} and (ii) for multilayers, the number of successive dip-coating steps which were separated by 30 min drying in an oven (90 °C) in between two steps.

2.3. Characterization techniques

2.3.1. Powder characterization

The crystal structure information of the products was analyzed by X-ray powder diffraction (PANalytical X'Pert Pro instrument Cu $K_{\alpha1}$ = 1.54056 Å, $K_{\alpha2}$ = 1.54439 Å and 2θ range from 8° to 80°). The unit cell parameters were refined by structural profile matching using the Fullprof program package. The morphology of the particles was studied using transmission electron microscopy (TEMJEOL 2100 and JEOL 1400+ microscopes, Tokyo, JAPAN) working at 200 or 120 kV acceleration voltage, respectively.

The total scattering data, necessary for the pair distribution function (PDF) analyses, were collected at the high energy (76.7 keV - Q_{max} up to 40 $Å^{-1}$) XPDF i15-1 beamline of Diamond Synchrotron (United Kingdom) using the rapid access program. The samples were packed into 1.0 mm diameter glass capillaries and mounted on the beamline goniometer to perform the measurements at room temperature. Data sets were collected using a PerkinElmer 2D detector and processed with the DAWN and GudrunX software packages to obtain the differential correlation function (D(r)). These data were fitted in the real-space D(r) with the TOPAS v6 software package using a dQ-damping macro term of 0.075 [29]. Unit cell lattice parameters, beta angle, tungsten atomic site positions, and spherical crystallite domain diameter sizes were refined.

The optical properties of the resulting products were tested by UV–VIS diffuse reflectance spectroscopy at room temperature from 200 to 2000 nm using a Cary 5000s equipped with an integration sphere (spectral resolution: 1 nm and band length: 2 nm). Halon was used as a white reference. RGB (Red-Green-Blue) space colorimetric parameters were determined from the spectra using a two-step mathematic treatment. The first step consists in extracting the XYZ tri-stimulus values (defined by the CIE, 1964) from the integration (over the visible range, i.e. from λ = 380 nm up to 780 nm) of the product of x(λ), y(λ) or z(λ) functions (CIE – 1964) with the diffuse reflectance spectra function $X = \int x(\lambda).R(\lambda)d\lambda$. Then, we used the transfer equations defined by the CIE, 1976, to transform the XYZ space to the L*, a* and b* common three-color space parameters. To explore the surface electronic structure of the products a ThermoFisher Scientific K-ALPHA spectrometer was used for XPS surface analysis with an Al K_α monochromatic source ($h\nu$ = 1486.6 eV) and a 200 mm X-Ray spot diameter. A pressure of 10^7 Pa was reached in the chamber when transferring the powders pressed onto copper tape. The full spectra (0–1100 eV) were obtained with constant pass energy of 200 eV and high-resolution spectra at constant pass energy of 40 eV. Charge neutralization was applied during analysis. High-resolution spectra of W4f were quantified and/or fitted using the AVANTAGE software provided by ThermoFisher Scientific (Scofield sensitivity factors used for quantification).

2.3.2. Film characterization

Before the electrical characterization, the device was prepared in this

way: 1- The film was masked using our Kapton® designed mask (2 × 2 cm with a spacing of 1.5 mm between the electrodes), 2- Then, the film was sputtered by gold to form the electrode by using a conventional sputtering instrument (BIO-RAD SEM Coating Unit PS3, BIO-RAD Laboratories Ltd. Hercules, CA, USA), 3- At the end, the mask was eliminated and kept for multiple usages. The process is summed up in Fig. 1. The four-point probe method was employed to measure the device's resistivity. The method requires the measurement of sheet resistance (Rs) and thickness (t) to calculate the bulk resistivity as $\rho = Rs \times t$ [30]. In the four-point probe method, the sheet resistance is measured as $Rs = \pi/\ln(2) \times (V/I) \times tk$, where I is the current, V is the voltage, and k is a geometric correction factor that depends on the ratio of the dimensions of the sample to the spacing of the probes, which in our case can be approximated to the thickness of our films [31,32]. A Keithley source measurement unit (SMU) 2400 A together with the four-point probe setup was used to measure the resistivity of all the samples coupled with photoconductive tests (illumination condition). The irradiation conditions were accomplished using a UV Hg-lamp (Vibert Lourmat 8. LC) at a monochromatic wavelength of 365 nm. The film was placed at 10 cm from 8 W tubes: the power per surface unit received by the sample is equal to 5.6 W/m^2, i.e. irradiance close to the UV-daylight irradiance in London daylight in September. The use of such low flux is to mimic the real condition a smart device (window or textiles) is exposed to under daily light in natural condition. To study the UV dose effect on photoconduction properties, the film was placed respectively at 7 and 5 cm, hence varying the power per surface received from the UV lamp. The power per surface was measured using a photoconductor connected to a spectrometer (AVANTES ULS4096CL) at each height separately. The signal collected from the spectrometer was integrated to calculate the approximate value of the power per surface. Finally, the thickness of the films and electrodes were determined using a WYCO NT1100 optical profilometer.

3. Results and discussion

3.1. The four different WO_3 nano-powders in a glimpse

To tune the oxygen substoichiometry of the as-prepared WO_3 nanopowders from the polyol process (WOR sample), this sample was dipped into an oxidizing aqueous solution, with $Cr_2O_7^{2-}$ polyanion as the oxidizer. The effect of different concentrations of the oxidizer agent (0.005, 0.01, 0.02 M) leading to WOX1, WOX2 and WOX3 samples, respectively on the blue WO_3 powder was examined. As shown in Fig. 2, a progressive change of the color from light blue (initial state) to the light yellow (oxidized state) is observed, all the more intense since the oxidizer concentration is high. It was noticed that a higher dosage of the oxidizer will cause a complete dissolution of the powder, so the maximum limit, which can be used was 0.02 M. Based on the abundant literature on tungsten oxide powder, higher oxidizer dosages result in lower surface oxygen substoichiometry of the nanoparticles, which lowers the intensity of the inter-valence band (W^{5+} to W^{6+} electron inter-atomic transfer) responsible for the red part of the visible range and near-infrared absorption. In L*a*b* color-space, the b* color parameter, relative to the blue– yellow color axis, so especially sensible to the powder color variation versus the oxidation, can be used to quantify the phenomenon (one can also use the luminosity L* directly linked to the maximum of reflectance, also an adequate parameter to quantify the oxidation phenomenon). The b* significantly evolves from −10.15 for the WOR raw powder to +30.14 (more yellow than blue) for the WOX3 most oxidized sample. On another side, the L* value increases for the as-prepared oxidized samples from 68.76, to 91.48 and then 92.06, as the oxidizer dosage increases.

These four samples were compared with one submicronic particle sized WO_3 powder (WOT sample) obtained from the calcination under air at 600 °C of the WOR sample. This powder exhibits a yellow color with L*a*b* parameters very close to the WOX3 sample.

3.2. Powder physicochemical characterizations

Firstly, the WOT obtained after a post-annealing under air exhibits from X-ray diffraction a $P2_1/n$ monoclinic structure, as the standard tungsten oxide structure (Fig. 3a). The profile matching of this air-annealed sample is achieved in the $P2_1/n$ space group using unit-cell parameters in good agreement with the numerous data reported in the literature [21,28,33]. The matching quality is good, and the reliability factors below 10%: Rexp = 5.16%; Rp = 9.47%. The WOT sample can be said to be a "standard" or "reference" WO_3 powder sample.

From the diffraction pattern peak profiles, it is possible to roughly determine the average crystal size of the particles with the help of Debye-Scherrer formula [32]: $t = K.\lambda/(\beta.\cos\Theta)$. In this equation, t is the mean size of the ordered (crystalline) domains, which may be slightly smaller or equal to the particle size, K the proportionality factor (also called the Scherrer's constant), which value is assumed to be $K = 0.9$ while β corresponds to the full width at half maximum (FWHM), λ the X-ray wavelength and θ the Bragg angle of the peak. It should be noted that the observed peak width is affected by the instrumental broadening as well as the broadening caused by the size effect (size broadening), so the instrumental broadening is subtracted to the total peak width to calculate the crystallite size. The calculated crystallite sizes were obtained equal to (i) 5.5 ± 1.6 nm for WOR, 3.2 ± 0.3 nm for WOX3 whereas for the WOT sample of monoclinic crystalline network, a size of 26.5 ± 3.5 nm is calculated. For WOR and WOX3 especially, this calculation on the crystallite size is a rough approximation since the XRD patterns show broad peaks, high background contribution besides peak intensity and furthermore a non-standard peak profile (with back asymmetry).

The broad diffraction peaks of the WOR and WOX3 samples are characteristic of small coherent domain sized crystallites, but some of the low 2θ peaks also exhibit a peak asymmetry (back asymmetry) which is more difficult to interpret. X-ray diffraction peak back asymmetry was

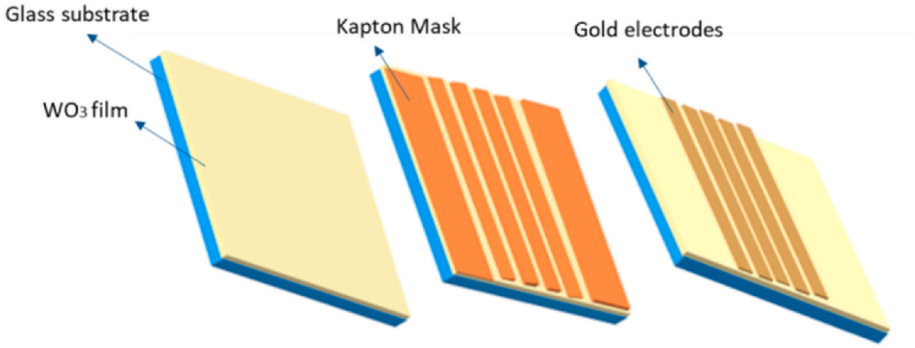

Fig. 1. Preparation of the photocoductor device.

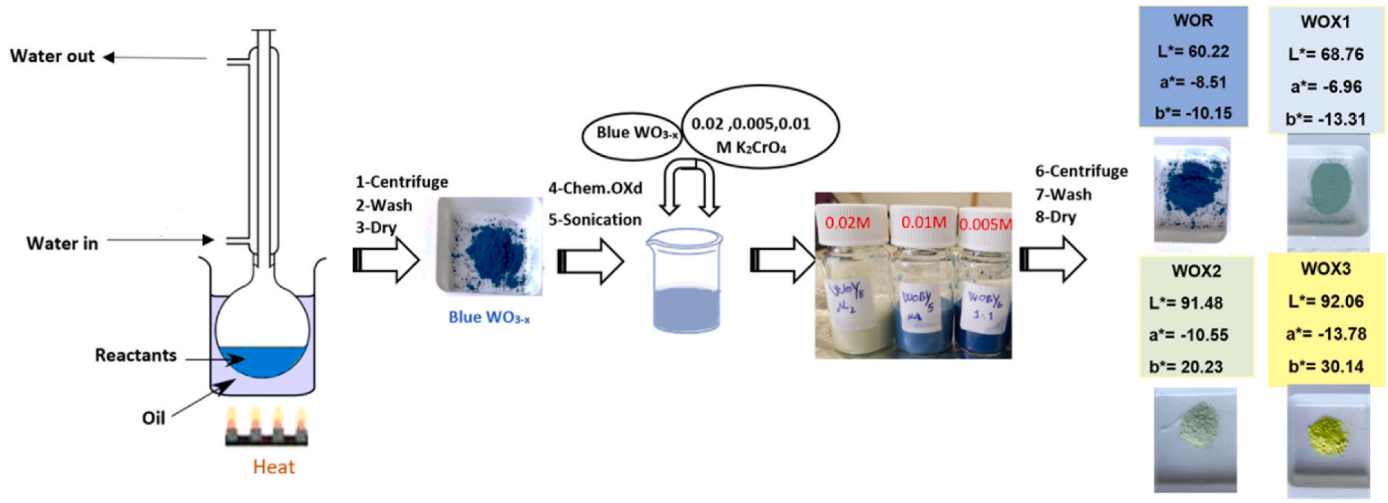

Fig. 2. Experimental flow starting from polyol precipitation and the oxidizing step parameters leading to the 4 studied samples from raw powder (WOR) to the most oxidized powder (WOX3).

already observed in nanoparticles of inorganic oxides prepared from polyol synthesis and exhibiting a gradient of lattice parameters from core to surface of the particles [34]. Thus, the raw and oxidized nanopowders seem to have a lattice parameter gradient. This can be explained considering two different hypotheses: (i) each nanometric particle constituting the blue and yellow samples exhibit a gradient of unit-cell parameters. It could be reasonably considered that this unit-cell parameter gradient is created from surface proximity (O/W ratio diverging from the surface to core of the crystallites); (ii) the different crystallites do not exhibit the same unit-cell parameters. Whatever the hypothesis, the difference in unit-cell parameters from one sample to another could be explained by slight differences in terms of chemical composition; for instance, different oxygen substoichiometry, or slight differences of surface strain contribution on unit-cell parameters depending on crystallite size. By varying the oxygen substoichiometry of raw powder either by chemical oxidation, a broadening of the main peak (100) with a back shoulder is observed as displayed using zoom into representative angular range (inset of Fig. 3b). The peaks become broader with the increase of oxidation condition as shown for the oxidized sample.

A solid-state chemistry model based on the bond-valence model of Brown et al. [35], can help to interpret the drastic modifications of the interatomic distances between the planes near the crystallite surface in comparison with the bulk material. A surface can be described as an area of missing bonds (with the subsequent excess of energy). The missing bonds around the surface atoms should cause a shortening of the bonds between these surface atoms and the atoms of the first underlayment. Indeed, the bond valence law expresses that the distance and the coordination number of an ion are linked by the equation:

$V = \sum_{i=0}^{n} bv_i = \sum_{i=0}^{n} \exp\left((r_0 - L_i)/0.37\right)$, where V is the valence of the ion (equal to the oxidation degree modulus: here = 6 for W^{+6}), bv_i is the bond valence of each bond implying the central ion, r_0 is an empirically determined parameter characteristic of the A−X bond (r_0 is tabulated equal to 1.917 Å for W^{+6}–O^{-2}bond), and L_i is the length of each i bond of the first coordination sphere. The valence is then a function of the number of bond lengths; when the coordination number I decreases (as on surface planes), each bond length should also decrease to maintain the V value to 6 for each W ion of the structure.

A Pauling−Brown bond relaxation approach was then adopted. In a first step, it was identified "natural" surface planes considering the easiest and only acceptable way (on a thermodynamic point of view) to produce stable tungsten oxide surface. First, it is straightforward to identify the (100) plane as natural cutting planes of the ReO_3-type structure since they are clearly the densest planes. Also, to maintain a $WO_{3.0}$ stoichiometric oxide (with only W^{6+} ions) one has to cut only half of the double bond between W^{+6} and O^{-2} forming so the adequate chemical pattern for the stoichiometric oxide surface. A second step consists into the attribution of the bond valence of the successive (100) bond layers from the surface to the bulk, layer by layer, in order to respect the ions' V valence value (V = 6 for W^{+6} ions). As shown in Fig. 3c, the calculation for the first, second and third layers are reported. These simple calculations of d spacing confirm our implication that, for our 5 nm WOR sample, the interatomic distance between surface atoms will be smaller than the equilibrium spacing between atoms in bulk material and could so be associated with a back asymmetry (short distance corresponding to large diffraction angles). The atoms at the surface of a particle (indeed at any free surface) perceive an environment that is distinctly different from that perceived by atoms within the bulk of the crystal (since there are no atoms to interact with on the outside of the free surface). For instance, a 3 nm crystallite (close to WOX3 and WOR) gets approximatively 55% of surface atoms (1st layer, only), whereas a 25 nm (close to WOT) crystallite exhibits a surface/core ratio of only 4.7%. Hence, the result is an effective surface tension on the surface of these particles, which implies that the atoms within the particles are under an effective force. Nonetheless, the variation of the d spacing between surface neighboring planes in regard of the bulk configuration is very low and such a hypothesis cannot explain such a huge back asymmetry of our oxide nanoparticles (in Fig. 3b inset are reported the angle positions associated with the three first calculated d spacing from surface). Obviously, considering now possible oxygen substoichiometry, cutting some W–O double bonds on the oxide surfaces will disrupt more drastically the d spacing configuration. Also, the WOX3 sample, which is without any doubt with a very low oxygen substoichiometry from its yellow color, exhibits the largest and most asymmetric X-ray diffraction peak. Hence, to explain the observed peak profiles as originating from a surface perturbation combined to their nanometric size seems inconclusive, PDF analysis of selected samples (WOT as reference, WOR and WOX3) provides additional details on atomic organization and coherent domain size, which is related to the maximum distance were peaks are observed. Differential correlation functions D(r) obtained, refined models, and difference curves displayed from PDF measurements performed on the three powders are presented (Fig. 3 d,e,f) in the 1.5−25 Å range. As expected, the WOT sample exhibits a monoclinic framework with the $P2_1/n$ space group and the coherent domain is largely exceeding the range of 1.5–25 Å, which is in good agreement with a crystallite size of 26.5 nm calculated with Debye-Scherer equation on XRD data. Regarding the WOR and WOX3 samples, a maximum distance where peaks are observed is close to the limit of the

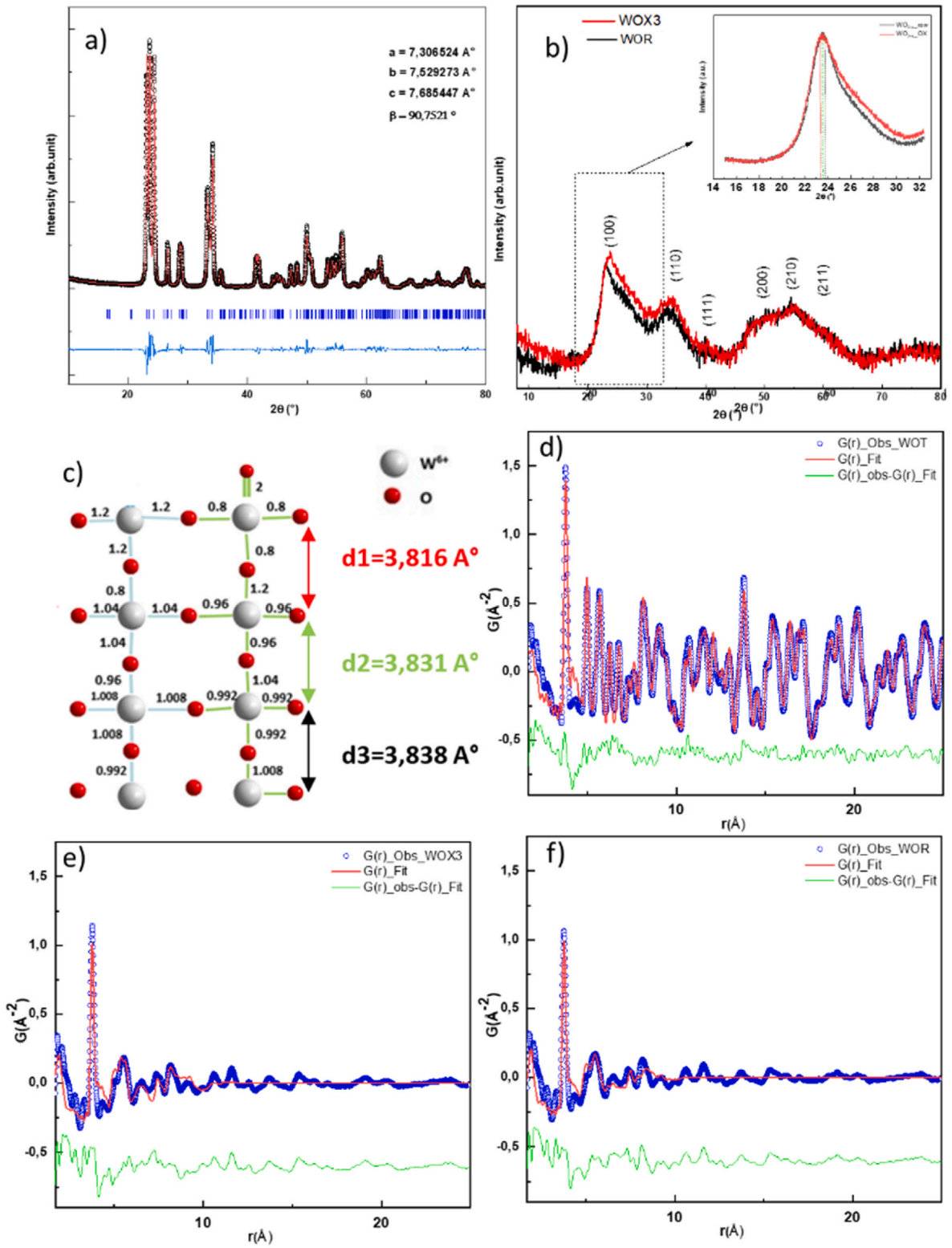

Fig. 3. a) XRD with profile pattern matching refinement for WOT, b) XRD pattern of WOR and WOX3 powders with a specific zoom on (100) peak. Representation of experimental, calculated and difference PDF G(r) curves for: d) WOT, e) WOX3 and f) WOR.

25 Å range. This value is a bit smaller than the crystallite diameters obtained from Debye-Scherer equation: 5.5 nm for WOR and 3.2 nm for WOX3, but remains consistent with regards to XRD data quality. However, we were able to fit the PDF data only with the $P2_1/n$ space group and only up to 10 Å, while adding a cubic space group did not improve the quality of the fit. This indicates that, unlike observations made with XRD, the building blocks of the WOR and WOX3 samples are closer to monoclinic structure than of a cubic one in the first coordination shells but the network distortion becomes so important after 10 Å that conventional crystal structure refinement fails. In this case, a deeper study could be conducted regarding structural modeling to solve the atomic organization. Nevertheless, focusing on the first coordination shells

where the fit is still matching, we can extract some information. Clearly, the XRD peak back-asymmetry, previously observed on both the later samples, originates from the (iso- or anisotropic) distribution of lattice parameters. The monoclinic distortion of the three studied samples can be quantified from different point of views. For illustration, we based the discussion on the unit-cell distortion (*UCD*) in regard of the pseudo-cubic equivalent unit cell [29]: $UCD = [(a_m\text{-}a_0)^2 + (b_m\text{-}a_0)^2 + (c_m\text{-}a_0)^2]^{1/2}$, with a_m, b_m and c_m: the monoclinic parameters extracted from pdf, and a_0: the pseudo-cubic cell parameters calculated as the cubic root of the monoclinic volume extracted from the PDF; *i.e. UCD* corresponds to the standard deviation in between the monoclinic and pseudo-cubic unit-cells. Also, it can be proposed for discussion the tungsten ion average out of centering (W_{OC}), considering the two Wyckoff positions, again in regard of the pseudo-cubic symmetry; *i.e.* the W_{OC} corresponds to the standard deviation of the two tungsten positions regarding the (0.25, 0, 0.25) and (0.25, 0, 0.75) reference in-cubic positions. Table 1 lists a summary of the refined parameters against the D (r) functions, including *a*, *b*, *c* and *beta* unit-cell parameters as well as the W cation positions. Also, *UCD* and W_{OC} calculated distortion factors are depicted in last column. For both distortion calculation assessments, monoclinic distortion amplitude is growing from WOR to WOT with WOX3 having intermediate values in between the raw blue powder and the post-annealed under air yellow sample. In other words, it means that if the monoclinic distortion is significantly decreased from the obtaining of very small crystallite size (comparison of WOR and WOX3 in regard of WOT), the effect of the surface re-oxidation clearly decreases these surface effects (WOX3 in regard of WOR).

TEM micrographs of the different samples are reported on Fig. 4. The WOT size distribution shows significantly larger isotropic particles of about 28 nm average diameter (Fig. 4c). This measurement is in good agreement with XRD and PDF analyses for which it was shown average size of 25 nm. The WOR and WOX3 samples present very small particles (Fig. 4a,b) with a size around 3 nm, difficult to distinguish from each other. The particle size distribution width is quite narrow (between 2 and 4 nm), but the agglomeration of the particles and their superimposition tend to limit the accuracy of the particle size distribution calculation. This very small size is in good agreement with the previous discussion extracted from the X-ray diffraction patterns as well from PDF analyses.

XPS was used to analyze the surface composition. Firstly, the XPS spectra of the WOR, WOT, and WOX3 powders are compared (Fig. 5). Fig. 5a shows that the air annealing post-treatment produces the full oxidation of the tungsten ions up to + VI oxidation state. Indeed, the WOT spectrum is constituted only by two peaks, which were assigned without any doubt to the W^{6+} state ($4f^{7/2}$ peak at 36.02 eV and $4f^{5/2}$ at 38.35 eV) [36,37].

This sample (WOT) can thus be considered a reference demonstrating that no further reduction of W^{6+} to W^{5+} is occurring during the XPS spectrum acquisition; at least for this sample. However, the W_{4f} fitting of the WOX3 sample shows a residual signal of W^{5+}. The W^{5+} signal corresponds to the two relatively peaks located at 33.95 and 36.10 eV. In addition, the occurrence of W^{5+} inside this compound is not in coherence with the yellow color of the oxidized powder compared to the spectrum of WOT. The XPS results confirm the presence of a significant amount of W^{5+} ions on the surface of the WOR and WOX3 powders. On the other hand, the absence of W^{5+} ions in the air-annealed sample is in good agreement with its pale-yellow color. XPS characterization gives an estimation of the W^{5+} proportion on the powder surfaces. Indeed, it can be assumed that the W^{5+} content occurs with an increasing gradient from the bulk to the surface. This effect can lead to an overestimation of the W^{5+} content from XPS investigations. The estimation of the W^{5+} content is 0.16 and 0.13 in the WOR and WOX3 respectively.

Table 1
Structural parameters for the WOT, WOR and WOX3 samples, extracted from PDF analyses.

Sample	a_m(Å)	b_m(Å)	c_m(Å)	*beta angle* (°)
	x (W_1)	y (W_1)	z (W_1)	*UCD* (Å)
	x (W_2)	y (W_2)	z (W_2)	W_{OC}
WOT	*7.3075*	*7.534*	*7.688*	*90.8*
	0.2552	*0.0399*	*0.2843*	*0.271*
	0.2452	*0.0253*	*0.7813*	*0.0704*
WOR	*7.4013*	*7.5532*	*7.5822*	*92.74*
	0.2611	*0.0435*	*0.2666*	*0.137*
	0.2415	*0.0090*	*0.7622*	*0.0504*
WOX3	*7.4006*	*7.4592*	*7.6588*	*92.25*
	0.2627	*0.0344*	*0.2714*	*0.191*
	0.2412	*0.0096*	*0.7702*	*0.0536*

3.3. Powder optical properties

Before UV illumination, the optical spectra of the powders from diffuse reflection measurements are reported in Fig. 6a. Firstly, the WOT reference powder shows a strong UV–vis absorption as well as a quasi-total reflection window in the visible spectrum, up to nearly 90% reflection at 500 nm. The yellow color is explained by the occurrence of the tungsten oxide gap located on the frontier between the UV range and the visible range, inducing a slight absorption of the purple hues. Secondly, in the studied oxidized series, the comparison between the samples shows a progressive divergence in their reflectance spectra: the higher the oxidizer dosage, the lower the intensity of the $W^{5+} \rightarrow W^{6+}$ inter-valence charge transfer responsible for the visible-near infrared absorption (large absorption band centred at about 1-μm wavelength). Consequently, the maximum reflectivity percentage located at 480 nm increases from 18% for the WOR, to 36% for WOX1, to 48% for WOX2, and up to 70% for the WOX3. The luminosity L*, directly linked to this maximum of reflectance, can be used to quantify the phenomenon. As already reported in Fig. 2, the L* value increases for the three as-prepared samples from 88.76, to 91.48 and then 92.06, as the oxidizer dosage increases. But obviously, the evolution of color in between the samples is better characterized from the b* chromatic hue axis from yellow to blue: the b* parameter rises from −10.15 for the light blue WOR sample up to +30.14 for the WOX3, most oxidized sample. At 2000 nm, the comparison of the reflectivity percentage between the three samples exhibits the same behavior: with values varying from 10%, 19%, and 37% for WOX1, WOX2, and WOX3 respectively. The reflectance contrast (ΔR taken as equal to the reflectance difference in visible and IR range) between 500 and 2000 nm is 55% for WOX3, whereas it reaches less than 30% for the other two samples. Hence, the most oxidized samples, exhibit the best selectivity (high visible transparency but with high NIR absorptivity) for the use of these compounds as solar filters, *i.e.*, with the best contrast between the visible and near-infrared transmission.

Ex-situ diffuse reflectance on WOT, WOR, and WOX3 samples after 5, 10, 20, 40, 60 and 90 min of irradiation are performed and the results are presented in Fig. 6b. The reflectance (R%) of the powders *vs.* UV-light irradiation time on 350–2000 nm wavelength range is recorded and can be transformed in Kubelka-Munk ($K/S = (1\text{-}R)^2/(2 \times R)$) absorbance spectra. K/S transforms exhibit an intensity of the absorption phenomena proportional to the chromophore concentration and are so used for kinetic analysis.

While WOT does not exhibit any significant photochromic property, both the two WOR and WOX3 samples exhibit a photochromic effect mainly concentrated in the near-infrared part of the spectrum. As no photochromism is offered by the WOT sample, the reflectance evolution which is not visible is not displayed. The associated chromatic coordinates in L*, a*, b* space presented in Fig. 6b allow the comparison of the photochromic efficiency of the WOR and WOX3 samples from the optical contrast calculated between the non-irradiated and 90 min irradiated samples. Indeed, even if our samples exhibit a photochromic effect mainly concentrated in the near-infrared part of the spectrum, the

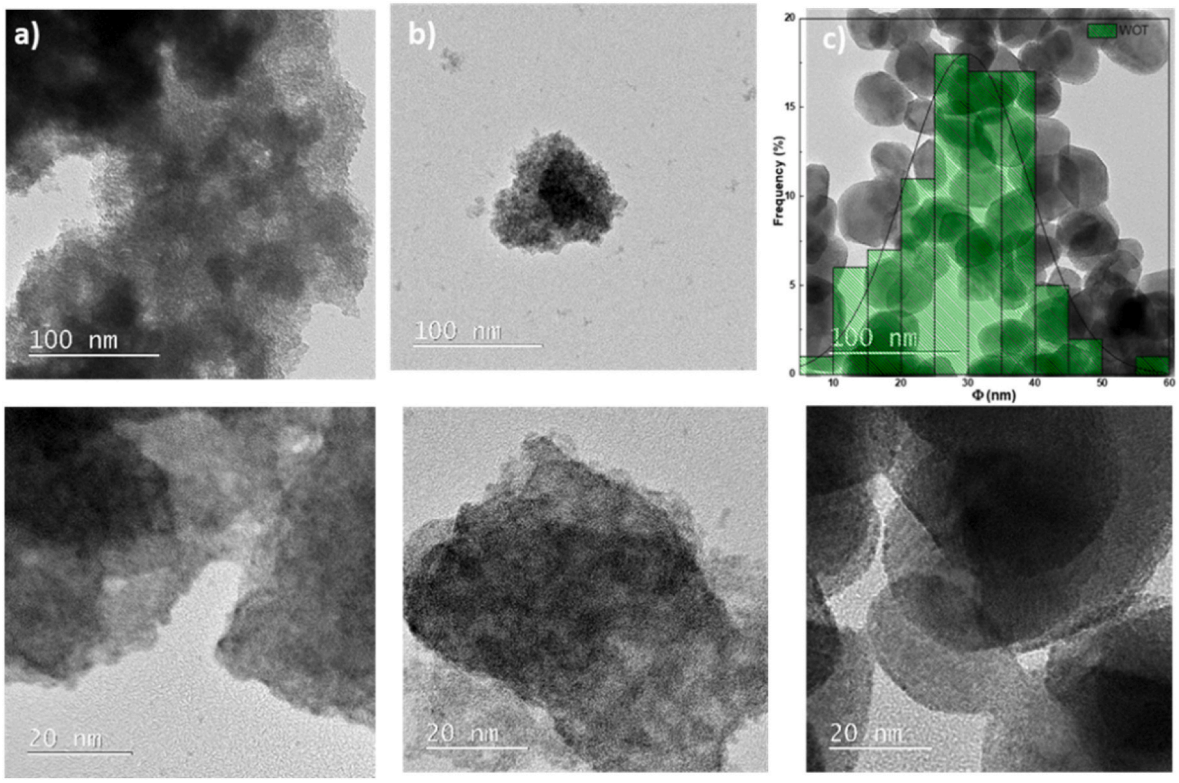

Fig. 4. Transmission Electronic Microscopy (TEM) micrographs of WO_3 powders: a) WOR, b) WOX3 and c) WOT.

impact of the inter-valence transfer in the visible range allows the observation of visible ΔC contrast:

$\Delta C = \sqrt{(\Delta b^{*2} + \Delta L^{*2} + \Delta a^{*2})}$. Photochromic contrasts are about 55.3 and 27.1 for WOX3 and WOR, respectively.

To better express the kinetic differences of the coloring against UV-irradiation between both the WOR and WOX3 samples, an exponential growth function was used to fit the experimental data, according to the equation: Y = A1.[exp(t/K1)]+Y0, with t in min, K1 is the characteristic time in min., A1 is the characteristic amplitude and Y0 is the y-offset (Fig. 6c). The values of the three parameters are shown in the inset, Fig. 6c. The WOR recorded a faster kinetic compared to WOX3 (4.4–9.1 min) which confirms the fact that the change of the oxygen sub-stoichiometry slows down the coloring kinetic behavior. For both powders, the coloring kinetic consists of photo-reduction of the surface cations from W^{+6} to W^{+5} then the surface after a short time becomes saturated with W^{+5} ions and this fast mechanism stops afterward.

3.4. Electrical characterization

Fig. 7a represents a prior study of the resistivity change for WOR films prepared from the coating of 4 or 10 layers (equivalent measured thickness 422 and 985 nm) WOR film as a function of irradiation time. The results indicate a lower resistivity value within the 10-layer film, which makes it the preferred number of layers for post photoconduction measurement (UV sensing): increasing the number of successive coatings beyond 10 layers has shown no supplementary gain of conductivity. Characterization of the photoconductor structures showed that the resistivity asymptotically decreases with irradiation time when the incident illumination power density is kept constant (5.6 W/m^2) for both 10-layers WOR and WOX3 films (Fig. 7b). The resistivity drastically decreased from 1.72×10^5 Ω cm to 8.62×10^2 Ω cm and from 4.71×10^4 Ω cm to 1.83×10^2 Ω cm for WOX3 and WOR films respectively as UV irradiation time increased with a change of color from light blue (WOR) or light yellow (WOX3) to dark blue for both films. As the photochromic phenomenon is based on the photoreduction of W^{6+} ions in W^{5+} defects at the particle surfaces, it appears obvious that the W^{5+}-W^{6+} intervalence charge transfer can be correlated with the resistivity mechanism as the increased number of charge carriers upon irradiation until the saturation, stabilizing the resistivity after 35 min. Nevertheless, the resistivity change can be also attributed to the interaction between the adsorption and desorption of oxygen molecules on the surface of the metal oxide layer which can explain the higher drop of resistivity of the oxidized film that contains higher oxygen anions compared to the raw film [38].

Due to the better resistivity contrast (difference between the two states: non irradiated and irradiated states), the WOX3 film was chosen to perform the photoconduction measurements. Herein, photoconduction means assessment of the change of resistivity versus UV irradiation; the collected current while 5V is applied with the 4 probes system varying with the UV irradiation is called photocurrent. The bias voltage was chosen in order to get some well-measurable photocurrent (few 10^{-6} A cm^{-2}). The photocurrent characteristics are measured at 365 nm UV-light illumination under three different light intensities: 5.6, 7.3, and 9.2 W/m^2 (surface powers were modified through the source – sample distance) and while switching of the irradiation between two states: ON (25 s of irradiation) and OFF (dark condition). It is important to insist on the very low surface power of the UV source we use in comparison to the literature. Since the as-prepared WO_3 films are hugely light sensible, they are able to detect UV micro-dose. Whatever the irradiation power, the WOX3 possesses a higher photocurrent (I_P) compared to the negligible dark current (I_{dark}) values. This confirms the generation of an increased number of photo-induced charge carriers during irradiation compared to dark condition. Furthermore, the photo-sensing properties of the photodetectors such as photo-responsivity (R), external quantum efficiency (EQE-indicated that the ratio of the number of charge carriers circulating in the circuit to the number of photons absorbed to generate them [39]), and photodetectivity (D^*, the ability of a photodetector to measure weak optical signals) are calculated using the equations reported in Fig. 7d:

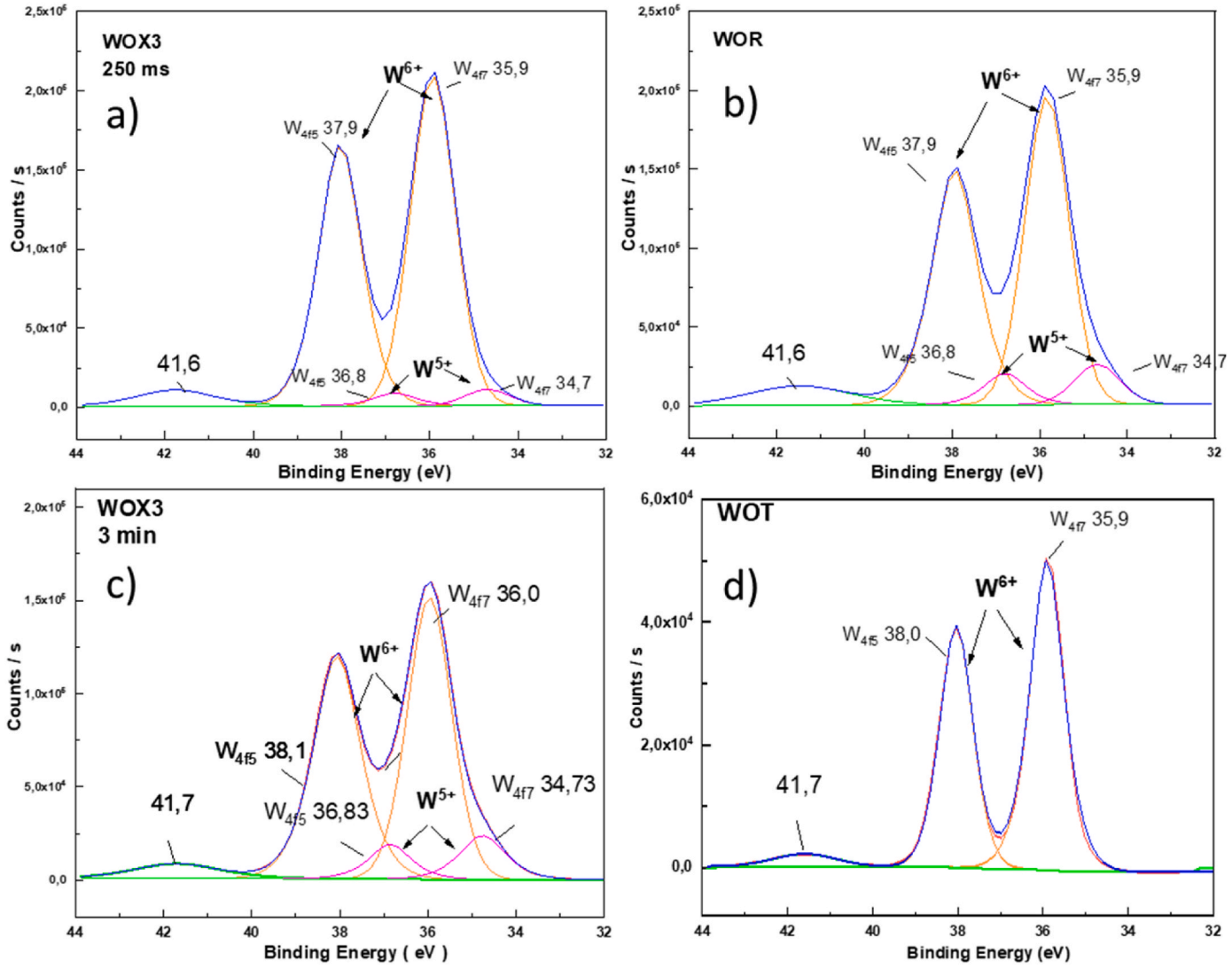

Fig. 5. High-resolution XPS spectra of W_{4f} and O1s: a) WOX3 with 250 ms analysis time, b) WOR, c) WOX3 with 3 min analysis time, and d) WOT.

$$R = \frac{I_P}{P_{in} \times A}, EQE = \frac{R.h.c}{e.\lambda}, D^* = \sqrt{\frac{A}{2.e.I_{dark}}},$$

where I_P donates the photocurrent value of the film (interpreted directly from Fig. 7c where I_P is the maximum current during the ON state), c represents the velocity of light, e gives the charge of an electron, h mentions Planck's constant, and A is the effective exposed area of the film to UV irradiation (where A is reduced to 2.5 mm^2 due to the excess coverage by the parallel metal electrodes on the semiconductor surface), which limits the exposure area of photoactive material for the incoming photons.

The responsivity and EQE behaviors as a function of irradiation power density are shown in Fig. 7d. The maximum responsivity of 0.37 A/W, EQE of 123.5%, and $D^* = 9.0*10^9$ Jones were obtained at the highest optical power density of 9.2 W/m^2. Surprisingly, the R and EQE were found to be increased as the optical power increased which can be explained by the improved photodetectivity D* in such low dose of UV. Same behavior was observed by Okada et al. [40], where they fabricated a high-quality AlGaN/GaN Schottky barrier photodetector. They studied the evolution of responsivity as function of power density and found that the obtained responsivity first increases with the increase of optical power density and reach a peak at an optical power density of 9 μW cm^{-2}. Thus, we believe that we did not yet reach the maximal responsivity and the observations still in the low domain of optical power density. Nevertheless, our goal is to study the sensitivity of the photodetector in low UV irradiance and we except to observe this behavior in this range of study. It has to be noted that the same response trend is shown on the 4-layer films, but with lowest photocurrents, showing a good reproducibility of the optical sensing possibilities.

The obtained WO_{3-x} film for UV photo-detection exhibits comparable performance when compared to many of the previous reports on such properties on metal oxide semiconductors as presented in Table 2.

The time-dependent photoresponse current increases along with the increment in UV light intensity with a slower decay behavior as the intensity of UV light is more intense. In each segment, the photocurrent did not saturate after irradiation but persisted to increase in the OFF state then decreased slowly during the dark conditions (decay phase). To better quantify the photo-response of the film, the photocurrent-time curve was modeled using a decay-exponential model, the fitting model was limited to the decay phase due to the persisting current in the OFF state, which makes it impossible to fit the rising segment for the third part. $K(t) = K0 + Nd.e^{-(t-tc)/\tau_d} \quad t > tc$.

$K(t)$ is the current at a given time, $K0$ is the y-asymptote, Nd is the decay amplitude of the exponential, tc is the time offset between exponential growth and decay, and τd is the time constant of the exponential decay term. From exponential curve fits, we obtain time constants listed in Table 3.

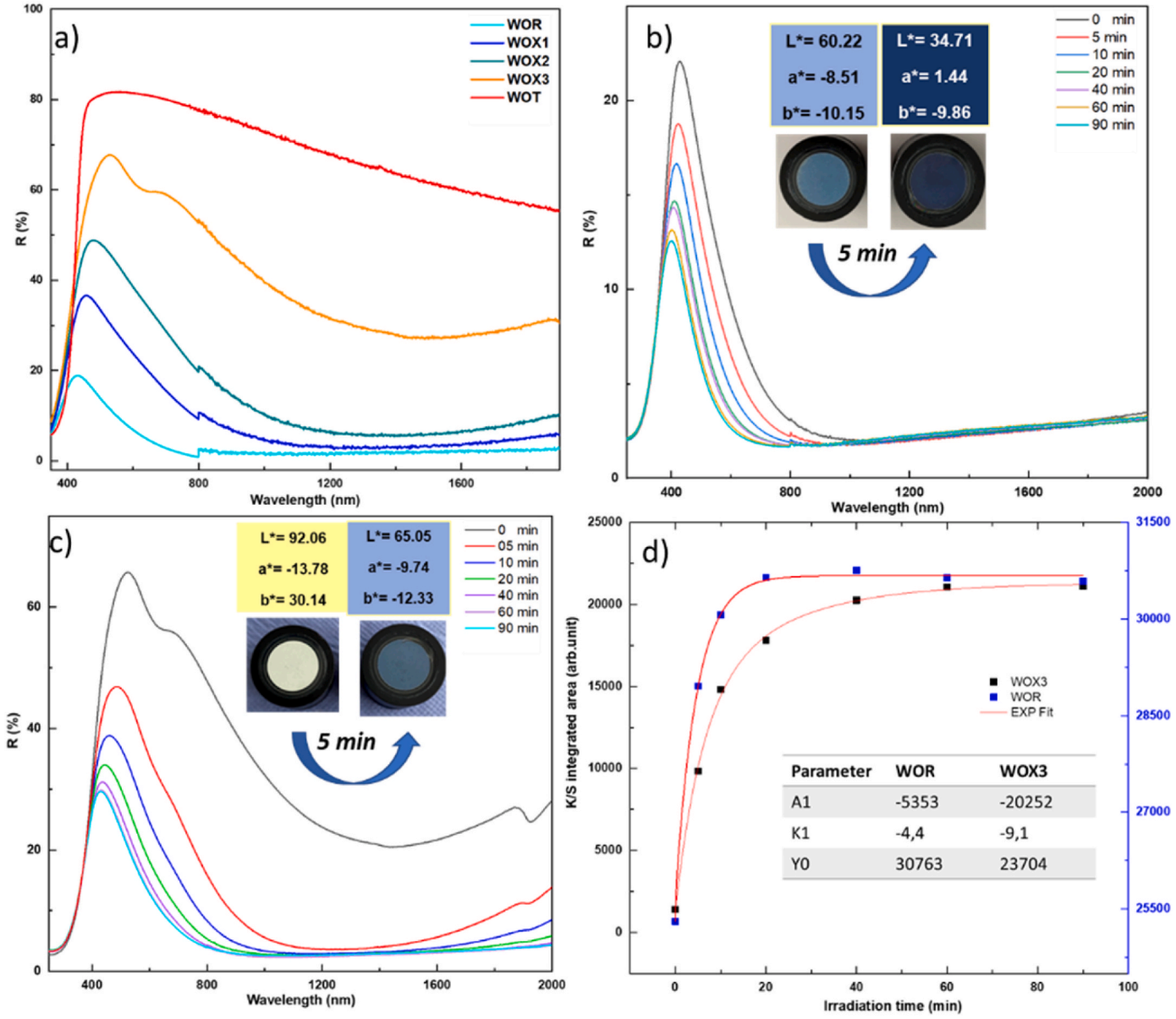

Fig. 6. a) Diffuse reflectance spectra of the studied powders. Photochromic study based on the reflectance evolution vs irradiation time for WOR (b), and WOX3 (c) samples. d) Evolution of the average K/S absorbance (400−2500 nm) vs irradiation time of both the WOR and WOX3 samples.

The slow decay behavior as revealed from kinetic fitting results in Table 3 (where the τd increases with the UV power intake) can be linked to the slow bleaching behavior of the film, as we have reported in a previous article [44]. Photochromism bleaching associated with photocurrent decay is due to the reoxidation of W^{5+} to W^{6+} by the oxygen in the air consuming longer time to return to the initial state. Also, we propose that the slow switching behavior originates from the persistent photoconductivity (PPC) effect intrinsic to WO_3 [45]. PPC phenomenon is related to metastable bulk defects located between shallow and deep energy levels considering that the oxygen vacancies can be excited to a metastable charged state after a structural relaxation [46]. In another approach, electron–hole separation near the surface can contribute to the PPC effect where the surface built-in potential separates the photo-generated electron–hole pairs and accumulates holes at the surface [20,47]. As shown in Fig. 7d the photo-responsivity increases with the UV power. Indeed, after illumination, the charge separation makes the electron–hole recombination difficult and originates PPC. The PPC effect causes the conductivity of WO_3 to increase slowly under illumination and the increased conductivity to persist even when the illumination is stopped. The PPC effect in WO_3 can also be discharged by heating the material to 155 °C and above, however, such an approach is impractical for photo-detection [42].

Into a glimpse, to go beyond our previous articles [19,44], the scheme of the sensing mechanism of such thin films is reported in Fig. 8. The phenomenon, is due to the reversible capability of the WO_3 thin films to exhibit a drastic change of conductivity through the $W^{5+} \rightarrow W^{6+}$ inter-valence charge transfer, which is allowed from electron/holes pair creation followed by charge depletion under UV light, and which is bleached under dark condition through the material reoxidation.

4. Conclusion

In conclusion, tuning the substoichiometry of the as-prepared WO_{3-x} nano-powders has been accomplished successfully via a reductive polyol precipitation followed by a partial chemical re-oxidation thanks to peptization into chromate aqueous solutions. W/O stoichiometric ratio has been analyzed by multiple techniques. The most re-oxidized samples exhibited the best selectivity (high visible transparency but with high

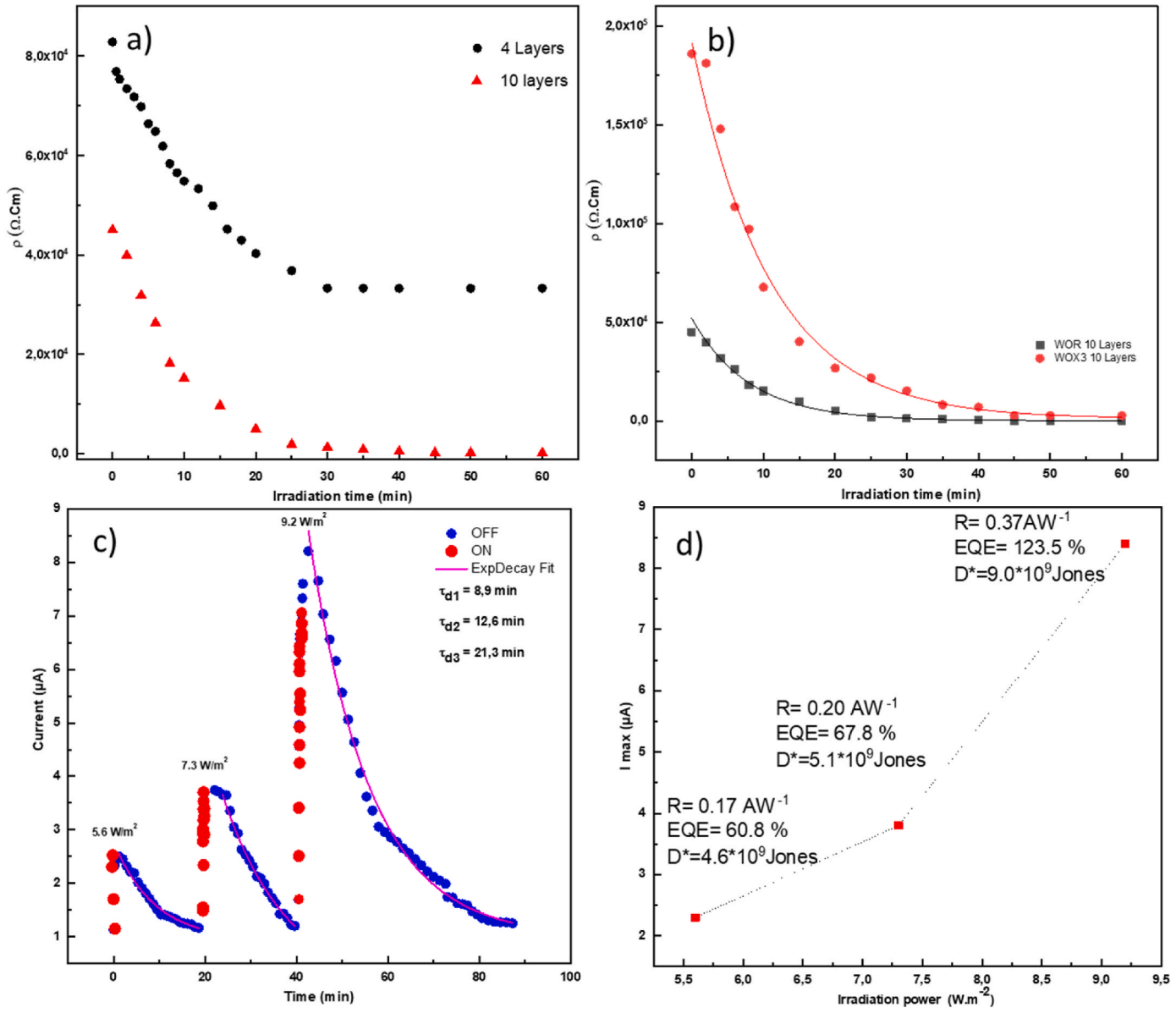

Fig. 7. a) Resistivity of the 4 and 10 layers WOR film as a function of irradiation time, b) Resistivity of the 10 layers WOX3 film as a function of irradiation time c) Time-dependent photo-response (current versus time) of the 10 layers WOX3 film measured under different irradiation. d) Maximum current as function of the UV dose with calculated R and EQE parameters for each point.

Table 2
Photosensitivity parameters of the as-prepared films compared with literature.

Sample	Photocurrent (μA)	R (A/W)	EQE (%)	REF
WO_{3-x}	*8.3*	*0.37*	*123.5*	*Presented work*
WO_3	*17.05*	*0.947*	*304.2*	[41]
WO_3	*0.18*	*0.000245*	-	[42]
CuO/Si	*0.96*	*0.000389*	*0.024*	[16]
MgO/ZnO	*7.1*	*40*	*146*	[43]

Table 3
Exponential decay fitting results for each UV irradiation power.

	5.6 mW/m²	7.3 mW/m²	9.2 mW/m²
τd (S)	*534*	*756*	*1278*
K0	*0.2*	*0.3*	*1.1*
Nd	*1.5*	*4.7*	*7.2*

NIR absorptivity) for the use of these compounds as solar filters, i.e., with the best contrast between the visible and near-infrared transmission. The coloring mechanism of the studied samples was governed mainly by fast photo-reduction of the surface cations from W^{+6} to W^{+5} associated with facile surface oxygen absorption-desorption. The detailed structural analysis of the WO_{3-x} nanocrystallites was performed coupling XRD pattern analysis, PDF analysis and TEM graphs. The crystal structure of all studied samples can be described in terms of exhibiting a monoclinic framework with P21/n space-group but with monoclinic distortion maintained despite the obtaining of the very low crystallite size. In an applicative point of view, the UV photo-detection measurements yielded a good responsivity of 0.37 A/W and external quantum efficiency 123.5% even at a very low power density (9.2 W/m^2) of the UV illumination. The possibility to extract photo-induced current below the open circuit voltage, with tunable intensity versus the light irradiation time, opens new possibilities as the next generation of photo batteries providing future optimization of the device design can sufficiently amplify the extracted currents. These experimental results

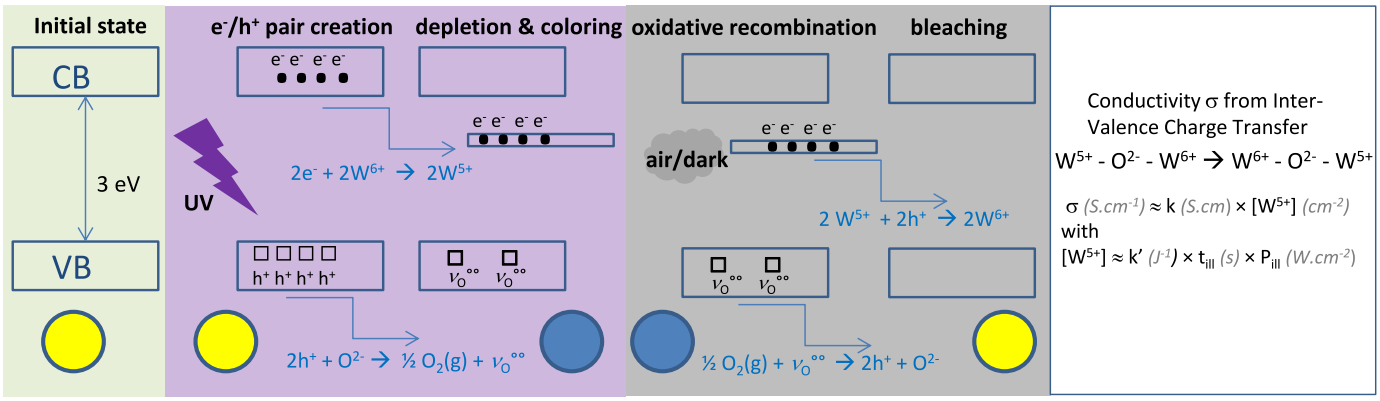

Fig. 8. UV-microdose sensing mechanism into a glimpse.

support that WO_{3-x} films could exhibit a promising usability in different optical applications such as smart window, optical filters and UV detectors.

CRediT authorship contribution statement

Yazan Badour: Synthesis of the WO3 NPs, 1st contributor to the characterizations. **Sylvain Danto:** Supervision, Co-direction of the studies, Writing – review & editing. **Mathieu Gonidec:** Electrical characterization. **Christine Labrugère:** Formal analysis. **Matthew R. Suchomel:** Formal analysis, characterizations and interpretations. **Gilles Philippot:** Formal analysis, characterizations and interpretations. **Manuel Gaudon:** Supervision, Co-direction of the studies, Writing – review & editing.

Declaration of competing interest

The authors declare the following financial interests/personal relationships which may be considered as potential competing interests: Manuel GAUDON reports financial support was provided by University of Bordeaux.

Data availability

No data was used for the research described in the article.

Acknowledgment

We acknowledge the support from the LIGHT S&T Graduate Program (PIA3 Investment for the Future Program, ANR-17-EURE-0027)". The authors also thank Diamond Light Source for mail-in beamtime access (proposal 27952), and the staff of beamline XPDF (I15-1) for assistance with PDF data collection.

References

[1] R. Diehl, G. Brandt, E. Salje, The crystal structure of triclinic WO_3, Acta Crystallogr. B 34 (1978) 1105–1111, https://doi.org/10.1107/S0567740878005014.
[2] B. Gerand, G. Nowogrocki, J. Guenot, M. Figlarz, Structural study of a new hexagonal form of tungsten trioxide, J. Solid State Chem. 29 (1979) 429–434, https://doi.org/10.1016/0022-4596(79)90199-3.
[3] P.M. Woodward, A.W. Sleight, T. Vogt, Structure refinement of triclinic tungsten trioxide, J. Phys. Chem. Solid. 56 (1995) 1305–1315, https://doi.org/10.1016/0022-3697(95)00063-1.
[4] K. Huang, J. Jia, Q. Pan, F. Yang, D. He, Optical, electrochemical and structural properties of long-term cycled tungsten oxide films prepared by sol–gel, Phys. B Condens. Matter 396 (2007) 164–168, https://doi.org/10.1016/j.physb.2007.03.031.
[5] E. Salje, The orthorhombic phase of WO_3, Acta Crystallogr. B 33 (1977) 574–577, https://doi.org/10.1107/S0567740877004130.
[6] W.L. Kehl, R.G. Hay, D. Wahl, The structure of tetragonal tungsten trioxide, J. Appl. Phys. 23 (1952) 212–215, https://doi.org/10.1063/1.1702176.
[7] P. Roussel, P. Labbé, D. Groult, Symmetry and twins in the monophosphate tungsten bronze series $(PO_2)_4$ $(WO_3)_{2\,m}$ $(2 \leq m \leq 14)$, Acta Crystallogr. B 56 (2000) 377–391, https://doi.org/10.1107/S0108768199016195.
[8] E. Gebert, R.J. Ackermann, Substoichiometry of tungsten trioxide; the crystal systems of $WO_{3.00}$, $WO_{2.98}$ and $WO_{2.96}$, Inorg. Chem. 5 (1966) 136–142, https://doi.org/10.1021/ic50035a033.
[9] F. Ali, N.D. Pham, L. Fan, V. Tiong, K. Ostrikov, J.M. Bell, H. Wang, T. Tesfamichael, Low hysteresis perovskite solar cells using an electron-beam evaporated WO_{3-x} thin film as the electron transport layer, ACS Appl. Energy Mater. 2 (2019) 5456–5464, https://doi.org/10.1021/acsaem.9b00547.
[10] H. Habazaki, Characterization of electrodeposited WO_3 films and its application to electrochemical wastewater treatment, Electrochim. Acta 47 (2002) 4181–4188, https://doi.org/10.1016/S0013-4686(02)00435-8.
[11] C.Y. Jeong, H. Watanabe, K. Tajima, Adhesive electrochromic WO_3 thin films fabricated using a WO_3 nanoparticle-based ink, Electrochim. Acta 389 (2021), 138764, https://doi.org/10.1016/j.electacta.2021.138764.
[12] Q. Liu, C. Hu, X. Wang, Hydrothermal synthesis of oxygen-deficiency tungsten oxide quantum dots with excellent photochromic reversibility, Appl. Surf. Sci. (2019).
[13] T. Kumpulainen, B. Lang, A. Rosspeintner, E. Vauthey, Ultrafast elementary photochemical processes of organic molecules in liquid solution, Chem. Rev. 117 (2017) 10826–10939, https://doi.org/10.1021/acs.chemrev.6b00491.
[14] Y. Badour, S. Danto, S. Albakour, S. Mornet, N. Penin, L. Hirsch, M. Gaudon, Low-cost WO_3 nanoparticles/PVA smart photochromic glass windows for sustainable building energy savings, Sol. Energy Mater. Sol. Cells 255 (2023), 112291, https://doi.org/10.1016/j.solmat.2023.112291.
[15] S.K. Deb, Optical and photoelectric properties and colour centres in thin films of tungsten oxide, Phil. Mag. 27 (1973) 801–822, https://doi.org/10.1080/14786437308227562.
[16] B. Cook, Q. Liu, J. Butler, K. Smith, K. Shi, D. Ewing, M. Casper, A. Stramel, A. Elliot, J. Wu, Heat-assisted inkjet printing of tungsten oxide for high-performance ultraviolet photodetectors, ACS Appl. Mater. Interfaces 10 (2018) 873–879, https://doi.org/10.1021/acsami.7b15391.
[17] Y. Badour, S. Danto, C. Labrugère, M. Duttine, M. Gaudon, Cu-doped and un-doped WO_3 photochromic thin films, J. Electron. Mater. 51 (2022) 1555–1567, https://doi.org/10.1007/s11664-021-09389-3.
[18] Y. Badour, S. Danto, C. Labrugère, M. Duttine, M. Gaudon, Cu-doped and un-doped WO_3 photochromic thin films, J. Electron. Mater. 51 (2022) 1555–1567, https://doi.org/10.1007/s11664-021-09389-3.
[19] M. Bourdin, G. Salek, A. Fargues, S. Messaddeq, Y. Messaddeq, T. Cardinal, M. Gaudon, Investigation on the coloring and bleaching processes of WO_{3-x} photochromic thin films, J Mater Chem C Mater 8 (2020) 9410–9421, https://doi.org/10.1039/D0TC02170A.
[20] X. Dong, Y. Wei, J. Gao, X. Liu, L. Zhang, Y. Tong, Y. Lu, Efficient charge transfer over Cu-doped hexagonal WO_3 nanocomposites for rapid photochromic response, J. Photochem. Photobiol. Chem. 425 (2022), 113716, https://doi.org/10.1016/j.jphotochem.2021.113716.
[21] Y. Badour, S. Danto, C. Labrugère, M. Duttine, M. Gaudon, Cu-doped and un-doped WO_3 photochromic thin films, J. Electron. Mater. 51 (2022) 1555–1567, https://doi.org/10.1007/s11664-021-09389-3.
[22] O.L. Evdokimova, T.V. Kusova, O.S. Ivanova, A.B. Shcherbakov, KhE. Yorov, A. E. Baranchikov, A.V. Agafonov, V.K. Ivanov, Highly reversible photochromism in composite WO_3/nanocellulose films, Cellulose 26 (2019) 9095–9105, https://doi.org/10.1007/s10570-019-02716-2.
[23] J. Wei, X. Jiao, T. Wang, D. Chen, The fast and reversible intrinsic photochromic response of hydrated tungsten oxide nanosheets, J Mater Chem C Mater 3 (2015) 7597–7603, https://doi.org/10.1039/C5TC01350J.
[24] Y. Badour, V. Jubera, I. Andron, C. Frayret, M. Gaudon, Photochromism in inorganic crystallised compounds, Opt. Mater. X. 12 (2021), 100110, https://doi.org/10.1016/j.omx.2021.100110.
[25] H. Cui, M. Zayat, P.G. Parejo, D. Levy, Highly efficient inorganic transparent UV-protective thin-film coating by low temperature sol-gel procedure for application on heat-sensitive substrates, Adv. Mater. 20 (2008) 65–68, https://doi.org/10.1002/adma.200701960.

[26] D. Shao, M. Yu, J. Lian, S. Sawyer, Optoelectronic properties of three dimensional WO_3 nanoscale and its application for UV sensing, Opt. Mater. 36 (2014) 1002–1005, https://doi.org/10.1016/j.optmat.2014.01.010.

[27] K. Huang, Q. Zhang, F. Yang, D. He, Ultraviolet photoconductance of a single hexagonal WO_3 nanowire, Nano Res. 3 (2010) 281–287, https://doi.org/10.1007/s12274-010-1031-3.

[28] M. Bourdin, M. Gaudon, F. Weill, M. Duttine, M. Gayot, Y. Messaddeq, T. Cardinal, Nanoparticles (NPs) of WO_{3-x} compounds by polyol route with enhanced photochromic properties, Nanomaterials 9 (2019) 1555, https://doi.org/10.3390/nano9111555.

[29] A.A. Coelho, P.A. Chater, A. Kern, Fast synthesis and refinement of the atomic pair distribution function, J. Appl. Crystallogr. 48 (2015) 869–875, https://doi.org/10.1107/S1600576715007487.

[30] M. Naftaly, S. Das, J. Gallop, K. Pan, F. Alkhalil, D. Kariyapperuma, S. Constant, C. Ramsdale, L. Hao, Sheet resistance measurements of conductive thin films: a comparison of techniques, Electronics 10 (2021) 960, https://doi.org/10.3390/electronics10080960.

[31] I. Miccoli, F. Edler, H. Pfnür, C. Tegenkamp, The 100th anniversary of the four-point probe technique: the role of probe geometries in isotropic and anisotropic systems, J. Phys. Condens. Matter 27 (2015), 223201, https://doi.org/10.1088/0953-8984/27/22/223201.

[32] R. Gross, A. Marx, Festkörperphysik, Oledenbourg Wissenschaftsverlag, 2014, https://doi.org/10.1524/9783110358704.

[33] A.J. Antony, C. Joel, R.B. Bennie, S.M.J. Kala, J.R. Jemima, Enhancing the optical, temperature-dependent electrical and dielectric properties of WO_3 through Fe doping for optoelectronic applications, J. Mater. Sci. Mater. Electron. 34 (2023) 761. https://doi-org.docelec.u-bordeaux.fr/10.1007/s10854-023-10109-2.

[34] I. Trenque, S. Mornet, E. Duguet, M. Gaudon, New insights into crystallite size and cell parameters correlation for ZnO nanoparticles obtained from polyol-mediated synthesis, Inorg. Chem. 52 (2013) 12811–12817, https://doi.org/10.1021/ic402152f.

[35] I. David Brown, The chemical bond in inorganic chemistry, J. Mater. Sci. 52 (2017) 9959–9962.

[36] T.H. Fleisch, G.W. Zajac, J.O. Schreiner, G.J. Mains, An XPS study of the UV photoreduction of transition and noble metal oxides, Appl. Surf. Sci. 26 (1986) 488–497.

[37] J. Díaz-Reyes, R. Castillo-Ojeda, M. Galván-Arellano, O. Zaca-Moran, Characterization of WO_3 thin films grown on silicon by HFMOD, Adv. Condens. Matter Phys. 2013 (2013) 1–9, https://doi.org/10.1155/2013/591787.

[38] K. Huang, Q. Zhang, Giant persistent photoconductivity of the WO_3 nanowires in vacuum condition, Nanoscale Res. Lett. 6 (2010) 52, https://doi.org/10.1007/s11671-010-9800-1.

[39] S. Lany, A. Zunger, Anion vacancies as a source of persistent photoconductivity in II-VI and chalcopyrite semiconductors, Phys. Rev. B 72 (2005), 035215, https://doi.org/10.1103/PhysRevB.72.035215.

[40] M. Kumar, C.Y. Lee, H. Sekiguchi, H. Okada, A. Wakahara, Demonstration of a large-area AlGaN/GaN Schottky barrier photodetector on Si with high detection limit, Semicond. Sci. Technol. 28 (2013), 094005, https://doi.org/10.1088/0268-1242/28/9/094005.

[41] P.V. Karthik Yadav, B. Ajitha, Y.A.K. Reddy, V.R. Minnam Reddy, M. Reddeppa, M.-D. Kim, Effect of sputter pressure on UV photodetector performance of WO_3 thin films, Appl. Surf. Sci. 536 (2021), 147947, https://doi.org/10.1016/j.apsusc.2020.147947.

[42] J.M. Wu, W.E. Chang, Ultrahigh responsivity and external quantum efficiency of an ultraviolet-light photodetector based on a single VO_2 microwire, ACS Appl. Mater. Interfaces 6 (2014) 14286–14292, https://doi.org/10.1021/am503598g.

[43] G. Liu, M. Zhang, D. Zhang, X. Gu, F. Meng, S. Wen, Y. Chen, S. Ruan, Effects of growth substrates on the morphologies of TiO_2 nanowire arrays and the performance of assembled UV detectors, Appl. Surf. Sci. 315 (2014) 55–58, https://doi.org/10.1016/j.apsusc.2014.07.115.

[44] M. Bourdin, G. Salek, A. Fargues, S. Messaddeq, Y. Messaddeq, T. Cardinal, M. Gaudon, Investigation on the coloring and bleaching processes of WO_{3-x} photochromic thin films, J Mater Chem C Mater 8 (2020) 9410–9421, https://doi.org/10.1039/D0TC02170A.

[45] C.-C. Lin, W.-H. Lin, Y.-Y. Li, Synthesis of ZnO nanowires and their applications as an ultraviolet photodetector, J. Nanosci. Nanotechnol. 9 (2009) 2813–2819, https://doi.org/10.1166/jnn.2009.008.

[46] S.M.-L. Pfaendler, A.J. Flewitt, High-resistivity metal-oxide films through an interlayer of graphene grown directly on copper electrodes, Graphene Technol 3 (2018) 11–18, https://doi.org/10.1007/s41127-017-0016-3.

[47] Y. Nukui, N. Srinivasan, S. Shoji, D. Atarashi, E. Sakai, M. Miyauchi, Vertically aligned hexagonal WO_3 nanotree electrode for photoelectrochemical water oxidation, Chem. Phys. Lett. 635 (2015) 306–311, https://doi.org/10.1016/j.cplett.2015.07.006.